



# Experimental investigations of flow and thermal behavior of wall confluent jets as a heating device for large-space enclosures

Gaspar Choonya<sup>a,\*</sup>, Ulf Larsson<sup>a</sup>, Bahram Moshfegh<sup>a,b</sup>

<sup>a</sup> University of Gävle, Department of Building Engineering, Energy Systems, and Sustainability Science, Sweden

<sup>b</sup> Linköping University, Department of Management and Engineering, Division of Energy Systems, Sweden

## ARTICLE INFO

### Keywords:

Experimental study  
Parametric study  
Wall confluent jets  
Core zone of the wall confluent jets  
Response surface methodology  
Large-space enclosure heating

## ABSTRACT

The study aimed to explore the effects of inlet air temperature, outdoor air temperature, inlet bulk velocity, and the number of nozzles on wall confluent jets (WCJ) propagating along an external cold wall in a large space enclosure such as a greenhouse. A combination of experimental study and Response surface methodology has been used to predict the flow and thermal behavior of the WCJ for the studied cases. Box-Behnken design was used to determine the case matrix for four of the above-mentioned vital variables for non-isothermal cases. The experimental study employed constant current anemometers to measure the velocity and temperature of the WCJ. Results showed that the WCJ attached to the wall under both isothermal and non-isothermal conditions. This flow behavior suggests that the WCJ can be used to heat the external facades of large-space enclosures. All the stated variables were critical to the decay factor and decay rate of maximum velocity, albeit at varying levels. The velocity decayed faster with an increase in the inlet bulk velocity and outdoor air temperature. It also decayed faster as the number of nozzles and inlet air temperature decreased. The external wall surface temperature and the wall-heating effect increased as the momentum of the jet increased. The surface temperature on the external wall was most influenced by the inlet air temperature and least by the number of nozzles. Correlations of the second-order polynomial for the Response surface models that estimate the rate of velocity decay and temperature on the external wall were obtained.

## 1. Introduction

The building sector accounts for about 40% of the total final energy use in most developed countries and contributes about 36% of greenhouse gas emissions [1–3]. In developed countries, HVAC systems use about 50% of the total building energy supply, which is estimated to be 10–20% of the national energy use [4–6]. Large-space enclosures are characterized by large spans, large floor areas, high ceilings, and large volumes [7] and energy use per floor heated area is higher compared to residential buildings. Greenhouses possess all the features of large-space enclosures in addition to having transparent envelopes and a direct connection to the outdoor environment. Energy use for greenhouse heating stands for 65–85% of the total energy use in the greenhouse for countries in cold climates [8,9]. High building energy use contributes to the high global energy demand that increases the use of primary energy. About 80% of the total global energy supply comes from fossil fuels which account for over 65% of the total global greenhouse gas emissions

(GHG) [2]. GHG emissions contribute to global warming, climate change, and environmental pollution. Thus, high energy use in commercial greenhouses based on fossil fuels contributes to carbon dioxide and other GHG [10–12]. The high energy costs inhibit year-round greenhouse agricultural activities, increase the cost of production, and reduce profits for the farmer [9,13].

Underlying factors that contribute to high energy use in buildings include building size, orientation, location, environmental factors, weather conditions, and building envelope and architectural design. Greenhouse building envelopes are made of glass or plastic, which has low thermal mass and heat storage capacity. Greenhouses require transparent envelopes to let sunlight indoors for plant growth. Transparent building envelopes entail insufficient insulation, which causes significant heat transfer through the building envelope in cold climates [7]. The building envelope influences the energy performance of the building because it determines the exchange of energy between the indoor and outdoor environments. Insufficiently insulated building envelopes can account for up to 40% of heat loss in winter [14]. Thus,

Abbreviations:  $U^*$  decay, Velocity decay factor [-].

\* Corresponding author.

E-mail address: [Gaspar.Choonya@hig.se](mailto:Gaspar.Choonya@hig.se) (G. Choonya).

<https://doi.org/10.1016/j.buildenv.2023.110282>

Received 27 December 2022; Received in revised form 24 February 2023; Accepted 6 April 2023

Available online 10 April 2023

0360-1323/© 2023 The Authors. Published by Elsevier Ltd. This is an open access article under the CC BY license (<http://creativecommons.org/licenses/by/4.0/>).

**Nomenclature**

$d_s$	Effective source diameter of nozzles [m]
$d$	Inside diameter of nozzle [m]
$E$	Space between two adjacent nozzles [m]
$T_{wall}$	Wall temperature [°C]
$T_{WCJ}$	Wall-based confluent jets temperature [°C]
$T_{in}$	Inlet air temperature [°C]
$T_{out}$	Outdoor air temperature [°C]
$U_b$	Inlet bulk velocity [m/s]
$n$	Number of rows of nozzles [–]
$U_{max}$	Streamwise maximum air velocity [m/s]
$U_{max0.5}$	Half of the streamwise maximum air velocity [m/s]
$Ar$	Archimedes number [–]
$g$	Gravitational acceleration [m/s <sup>2</sup> ]

**Abbreviations**

CJ	Confluent jets
CJCZ	Confluent jets core zone
CZ	Core zone
WCJ	Wall confluent jets
WCJV	Wall confluent jets ventilation
RSM	Response surface methodology
RS	Response surface
HVAC	Heating, ventilation, and air conditioning system
GHG	Greenhouse gas emissions
CCA	Constant current anemometer
BBD	Box-Behnken design

**Greek letters**

$\beta$	Coefficient of thermal expansion (Equation (6)) [K]
---------	---

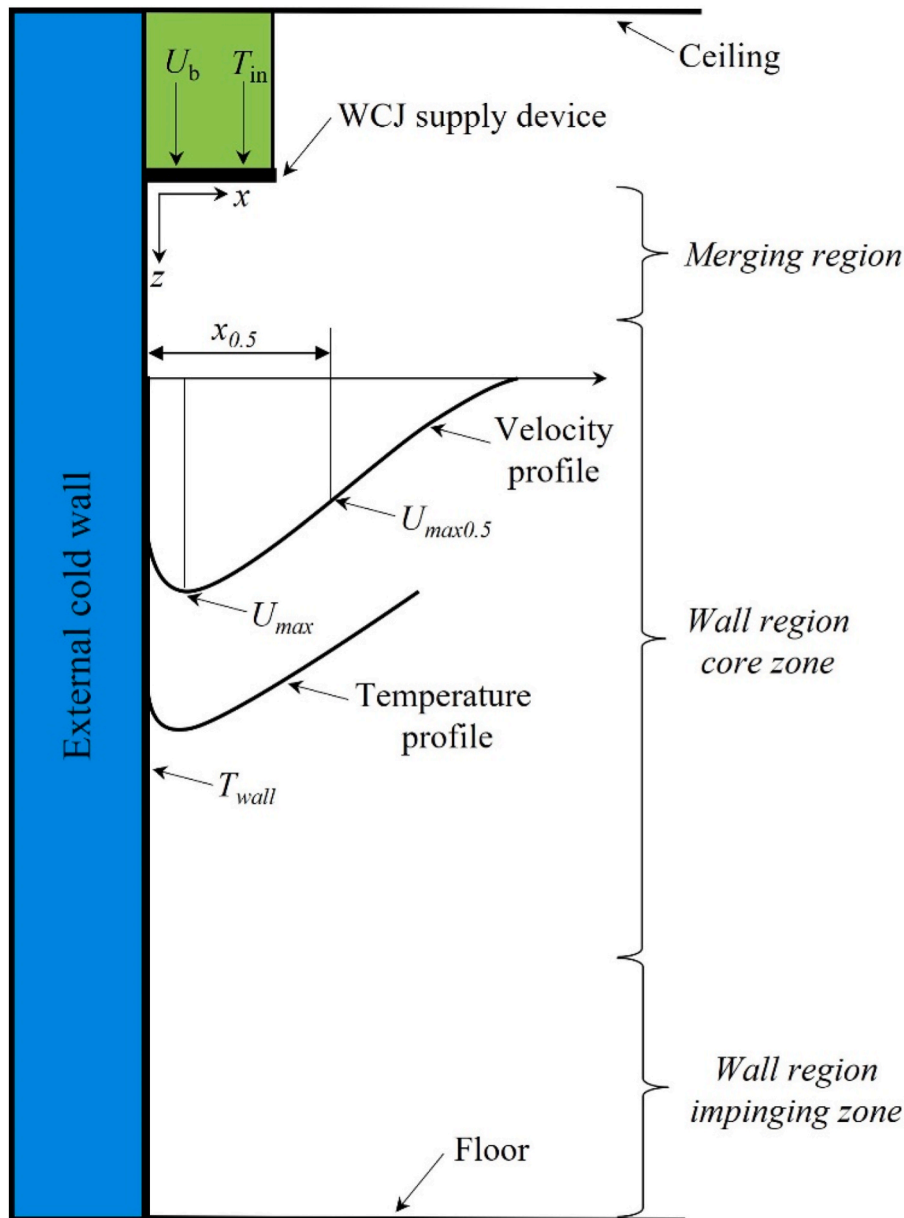


Fig. 1. Position of the WCJ supply air diffuser, regions of the WCJ, and characteristic velocity and temperature profiles in the core zone [19,26,27].

strategies such as insulating the building envelopes can reduce building energy use for space heating. However, proper insulation mechanisms should be applied to prevent obstructing sunlight transmission into the greenhouse. The current study proposes using WCJ to insulate an external cold wall of a typical greenhouse.

Confluent jets (CJ) is created from a matrix of circular air jets issuing from several nozzles in the same plane. Initially, the jets flow parallel to each other and later merge into a single jet at a certain distance downstream of the diffuser [15]. Several researchers have computationally and experimentally studied the flow characteristics of the CJ [15–25]. CJ penetrates deeper into the occupied zone than single free jets because they bundle together about the centreline and entrain less surrounding air [26]. CJ is applied in meteorology, air suppliers of ventilation systems [26,27], air curtains, combustion burners [28], fluid mixing, multipoint waste water diffusers, and pollutant dispersion and plume dilution from chimneys [19,29].

When CJ flow closer to a surface, they attach to the surface and form a wall jet known as WCJ [26]. Janbakhsh and Moshfegh [27] define a WCJ as a wall jet that is formed when individual air jets issuing from a CJs supply device coalesce into a single jet and attach to a proximal wall, and move downwards attached to the wall [27]. This flow behavior only allows the entrainment of air to take place on the room air side of the jet. As a consequence, a boundary layer forms on the wall surface, and shear layers of the fluid form within the jet on the room air side [15].

WCJ-based ventilation (WCJV) systems are widely used in various indoor environments [17,26,27,30]. Earlier studies indicate that the WCJV systems create better indoor air quality and thermal comfort, and have higher ventilation performance and energy efficiency than mixing ventilation and displacement ventilation systems [16,17,31,32]. WCJV have higher penetration into the occupied zone and greater horizontal spread over the floor than displacement ventilation systems [26]. WCJ has slower rates of velocity decay [15] and conserves momentum better than regular wall jets [26,33]. The high momentum conservation tendency of the WCJ makes it suitable for use in ventilation systems for larger spaces like classrooms [25], theoretical assumption indicates it can be used for heating greenhouse premises. Many non-isothermal studies conducted on the WCJ involved cooling applications where the temperature of the WCJ was lower than the temperature of room ambient air. Studies that assess the performance of WCJV when the WCJ is supplied at a higher temperature than the room air temperature are sparse. More research is required to understand the flow and thermal characteristics of the WCJ in heating applications.

Fig. 1 shows the characteristic velocity and temperature profiles of the WCJ. The position of the jet is designated by  $z$  and  $x$ , where  $z$  is the distance from the inlet air diffuser, and  $x$  is the distance from the wall surface into the room.

A previous study indicated that the flow behavior of WCJ is a combination of three regions, namely free jet, Coanda effect region, and wall region [26]. Other studies identified the primary and secondary regions as the flow regions of the WCJ [27,30]. The current study categorizes the flow regions of WCJ as the *merging jet region* and the *wall region* based on the location of the measurement zone and by inferring from previous studies [15,19,26,27]. The merging jet region lies closer to the air inlet diffuser and individual jets merge into a single jet. As the air jets issue from the inlet diffuser, they turbulently mix with the ambient air that causes significant velocity decay [34]. The jets combine into a single jet at the end of the merging region and attach to the wall due to the Coanda effect [26]. In the wall region, the merged jets flow downstream while attached to the wall. The wall region is made up of a confluent jets core zone (CJCZ) [19] and impinging zone [27]. The concept of CJCZ was also applied in the study of unconfined CJ [19]. Although the present study concerns confined CJ, it adopts the concept of CJCZ and calls it a core zone (CZ) because of similar flow behavior. The decay of the maximum streamwise velocity is rather low in the CZ [19,26,27]. Higher decay of the maximum streamwise velocity occurs in the impinging zone than in the CZ. The primary focus of the current study is on evaluating

the flow and thermal characteristics of WCJ in the CZ of the wall region.

Fig. 1 shows the characteristic velocity and temperature profiles of the WCJ in the CZ. The maximum streamwise velocity is located nearer the wall surface in CZ for smaller  $z$ . The location changes further into the room as the jet distance from the inlet air diffuser increases. This is due to more entrainment of room air as the jet propagates towards the floor. For a WCJ supplied at an inlet air temperature ( $T_{in}$ ), it flows downstream along the cold wall with a temperature ( $T_{WCJ}$ ) and affects the proximal wall by surface temperature designated as  $T_{wall}$ . Several studies have been conducted on CJ [16,18–21,24,35,36], but little focus has been made on the WCJ. Of the few studies on the WCJ, many concentrated on cooling applications. Studies that assess the performance of WCJV when the WCJ is supplied at a higher temperature than the room air temperature are sparse. More research is required to understand thoroughly the flow and thermal characteristics of the WCJ supplied at a higher temperature than the room air in heating applications. Research on the use of the overheated WCJ in heating applications in large enclosures is scarce. The current study explores the flow and thermal behavior of an overheated WCJ propagating along a cold wall mimicking an external wall in a typical greenhouse enclosure. The study seeks to address the application of the WCJ from cooling applications in domestic buildings to heating applications in non-human-occupied large spaces like greenhouses. The ability of the WCJ to attach to the proximal wall surface makes it theoretically suitable to be used for ‘insulating’ purposes. The current study uses an overheated WCJ as an ‘insulating’ layer on the plastic facades of a mock-up greenhouse. The air layer of the overheated WCJ on the enclosures’ inner surface will separate the outdoor and indoor environments, thus improving the energy performance of the building. Due to the rather moderate air temperature in the WCJ, waste heat (usually below 50 °C) from industrial processes can be used as a heat source.

The experimental study investigates the effects of parameters such as inlet air temperature ( $T_{in}$ ), outdoor air temperature ( $T_{out}$ ), inlet bulk velocity ( $U_b$ ), and the number of rows of nozzles ( $n$ ), on the flow and thermal behavior in the CZ of an overheated WCJ propagating along an external cold wall. The study used constant current anemometers (CCAs) to measure air velocity and temperature. It employed thermocouples to measure surface and air temperature in the test room and cooling chamber. Finally, it involved response surface methodology (RSM) to understand the effect of the stated parameters on the flow and thermal behavior of the WCJ.

## 2. Methods

### 2.1. Experimental setup

The experiment was conducted in a test room in the Laboratory of Ventilation and Air Quality at the University of Gävle, Sweden. The internal dimensions of the test room were 4.3 × 2.0 × 4.2 m. It was composed of three well-insulated inner walls and one external wall made of thermoplastic. The three well-insulated inner walls were composed of a 15 mm wood sheet, 35 mm air gap, 15 mm wood sheet, 190 mm insulation, and 5 mm wood sheet on the external side. The external wall was 4.2 m high and 2.0 m wide and was directly connected to a cooling chamber. The external wall was referred to as external cold wall because its connection to the cooling chamber and its height was selected to mimic the eave height of a greenhouse. There are different types of greenhouses, but the typical eave height of the Gable roof type is between 3.7 m and 4.9 m [37]. The thickness and  $U$ -value of thermoplastic material for the external wall were 0.016 m and 1.95 W/m<sup>2</sup>K, respectively. The floor and ceiling had an upper layer of wood and a 150 mm thick layer of mineral wool insulation and were covered by a layer of plastic sheet to minimize air infiltration. The walls, floor, and ceiling were insulated to minimize heat gain or heat loss. The cooling units in the cooling chamber were adjusted to create air temperatures of −10 °C, 0 °C, and 10 °C which represented varying wintery  $T_{out}$ . Air temperature

in the cooling chamber was maintained by a 1.8 kW Rivacold FTL016 cooling system with a cooling effect of  $-20\text{ }^{\circ}\text{C}$  at an ambient air temperature of  $32\text{ }^{\circ}\text{C}$ . The air was extracted from the test room through an air exhaust slot 1.7 m long and 0.08 m wide on the wall, that is, opposite the external wall. Fig. 2 (a) and (b) show the experimental setup used in the study.

The WCJ supply duct was 2 m long and 0.3 m wide with three sides made of wood and the fourth side which contained the nozzles made of stainless steel (WCJ supply device). The air supply device was mounted on the ceiling, close to and parallel to the external cold wall. Before the air from the supply duct entered the diffuser, it flowed through a plenum. The plenum, which was a 2 m long, and 0.27 m wide wooden box created uniform flow and maintained positive air pressure in the diffuser. The air from the plenum flowed into the WCJ supply device through a 0.05 m wide slot located on the side adjacent to the WCJ supply duct. The air was supplied into the test room through the nozzle plate whose face was 3.9 m above the floor and perpendicular to the external cold wall. Fig. 3 shows some details of the nozzle plate.

The dashed lines in Fig. 3 indicate hidden details of the WCJ supply device. The diameter of the nozzle opening and the space between two adjacent nozzles were  $d = 0.0058\text{ m}$  and  $E = 0.01056\text{ m}$ , respectively. Different nozzle configurations were obtained by varying  $n$  and maintaining a fixed number of columns ( $m = 62$ ). Thus,  $n = 8, 10$ , and  $12$  created the following nozzle arrays:  $8 \times 62$ ,  $10 \times 62$ , and  $12 \times 62$ , respectively. The length  $l$  of the nozzle plate was constant at 1.025 m while the width  $w$  varied according to  $n$ . For  $n = 8, 10$ , and  $12$ , the width  $w = 0.152\text{ m}$ ,  $0.184\text{ m}$ , and  $0.22\text{ m}$ , respectively.

#### 2.1.1. Supply air heating and airflow rate measurements

The air was supplied into the room through a 0.25 m diameter duct. The airflow rate was measured using the SwemaMan 80, with an accuracy of  $\pm 0.4\text{ Pa}$  for temperature range  $0\text{ }^{\circ}\text{C}$  to  $50\text{ }^{\circ}\text{C}$  by measuring the pressure difference across a mounted Diru 250 orifice plate. The airflow rate into the room was calculated using Equation (1).

$$q = k \sqrt{\Delta P_i} \quad (1)$$

Where,  $q$  [l/s], is the inlet airflow rate,  $k$  [–] is a characteristic constant of the orifice plate (used  $k = 45$ ),  $\Delta p_i$  [Pa] is the pressure difference across the orifice plate. The HVAC system with a heating effect of 7.5 kW was used to raise the temperature of the air to the required inlet air temperature level. Three  $T_{in}$  setpoints were used:  $30\text{ }^{\circ}\text{C}$ ,  $35\text{ }^{\circ}\text{C}$ , and  $40\text{ }^{\circ}\text{C}$ .

#### 2.1.2. Air temperature and velocity measurements of the WCJ using CCAs

The WCJ velocity and temperature were measured by in-house-made CCAs. The CCAs simultaneously measured air velocity and temperature. CCAs employed thermistors as sensors. Each CCA probe has two sensors, one for air temperature and the other for velocity measurements. The velocity sensor is a spherical Honeywell 111-202CAK-H02 thermistor of 0.3 mm diameter. Thermistors are temperature-sensitive resistors and both sensors are calibrated - temperature vs resistance, and calibration data are stored in a computer. The velocity thermistor is operated in the self-heating mode, which means that a current is forced through the thermistor to heat the sensor by joule heating. The velocity of the air is related to the heat transfer occurring as the heat from the heated sensor dissipates due to forced convection. Equations (2) and (3) show the heat transfer from the velocity sensor and the relation of the air velocity to the heat transfer for each measurement.

$$H = P_s / (T_s - T_a) \quad (2)$$

$$U = f(H) \quad (3)$$

Where  $T_a$  is the air temperature ( $^{\circ}\text{C}$ ),  $T_s$  is the temperature of the velocity thermistor ( $^{\circ}\text{C}$ ),  $P_s$  is the electrical power delivered to the sensor,  $H$  is the heat transfer,  $U$  is air velocity and  $f$  is a third-order polynomial.  $H$  is related to velocity by calibration to known velocities. Using the relationship described in Equation (3) and the stored calibration data, the velocity of the air was determined. The air temperature is in first place measured for calculation of velocity but is also available as an output. The sensors were calibrated for velocities between 0.5 and 20 m/s, with an accuracy of  $\pm 5\%$  with a time constant of 0.5 s at 0.5 m/s and 0.1 s at 20 m/s.

The CCA probes also contained a Thermometrics B43-K-5 temperature sensor that was calibrated for a temperature range of  $20\text{ }^{\circ}\text{C}$  to  $40\text{ }^{\circ}\text{C}$  with an accuracy of  $\pm 0.05\text{ }^{\circ}\text{C}$ . The CCAs were calibrated using a small open-circuit wind tunnel offering a stable and low-turbulent flow. The overall accuracy of the anemometers is  $\pm 10\%$ .

The CCAs were connected to a 32 multi-channel anemometer logger system and interfaced by LabVIEW version 2017. The anemometer logger system measures the electrical power delivered to each sensor and the dissipated power is calculated using the ohms law. Thermistor resistance vs. temperature is measured in the range of  $0\text{--}80\text{ }^{\circ}\text{C}$  in the logger system. The system has a voltage divider formed using a precision resistor ( $2\text{ k } 0.1\%$ ) and a precision voltage source based on reference voltage in the CCA provides a known voltage input to the divider. The voltage across the thermistor is measured using data acquisition systems with model number NI USB-9218 DAQ calibrated and supplied by

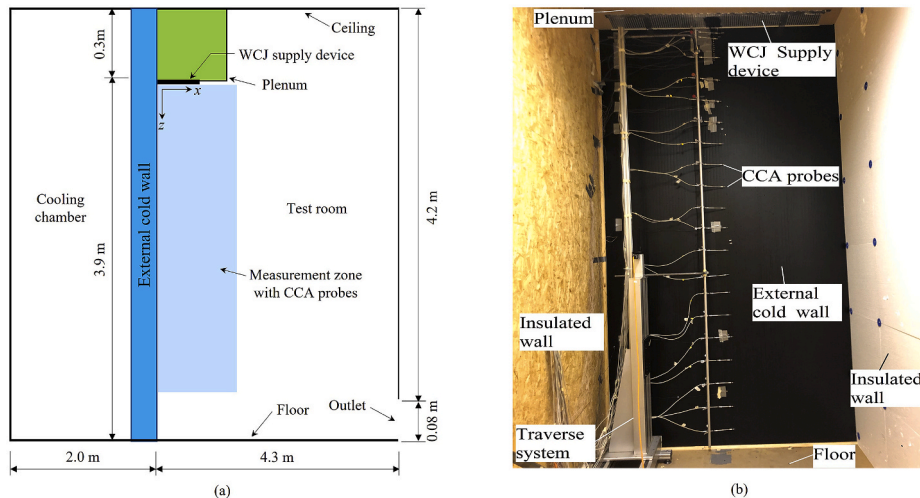


Fig. 2. Experimental setup of the study: (a) Side view of test room (b) setup of CCAs.



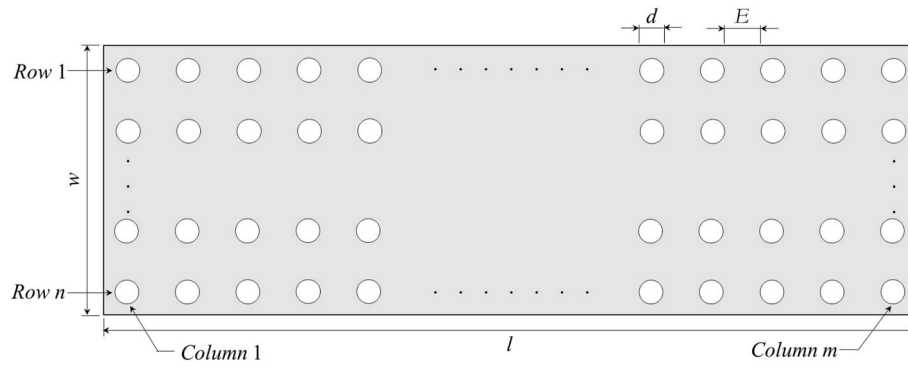


Fig. 3. WCJ supply device.

National Instruments Corporation.

Fig. 2(b) shows the setup of CCAs used to measure air velocity and temperature in the study. Cartesian coordinates were used to describe the position of the measurement point in the measurement zone. The  $z$ -axis is oriented along the external cold wall with a positive direction towards the floor, while the  $x$ -axis is perpendicular to the external cold wall and is positive towards the room center. The origin of the  $z$ -axis ( $z = 0$ ) is at the face of the nozzle plate and that of the  $x$ -axis ( $x = 0$ ) is at the inner surface of the external cold wall on the test room side. Twenty (20) CCA probes were mounted on a rigid steel rod which was attached to a traverse system. The 3D Dantec traverse system had a positioning accuracy of  $\pm 0.1$  mm and moved within the measurement zone. The measurement zone was bounded vertically by the lines  $x = 0.003$  m to  $x = 0.54$  m, and horizontally by  $z = 0.05$  to  $z = 3.6$  in the  $xz$  plane. The traverse system moved from near the cold wall starting at  $x = 0.003$  m to end at  $x = 0.54$  m from the external cold wall at an interval of 0.002 m. This movement allowed the air velocity and temperature to be measured at different points across the jet. The measurement zone is shown in Fig. 2(a). The measurement duration at each point was 20 s at a sampling rate of 200 samples per second. To measure the measure air velocity and temperature closer to the diffuser, two CCAs were installed within  $z = 0.1$  m. The first probe was placed at  $z = 0.05$  m and the second probe at  $z = 0.1$  m. The remaining eight (18) probes were placed at an interval of 0.2 m starting from  $z = 0.1$  m to  $z = 3.6$  m.

### 2.1.3. Air and surface temperature measurements using thermocouples

Air and surface temperatures were measured using T-type (copper-constantan) thermocouples with a measuring range of  $-200$  °C to  $350$  °C [38]. They were connected to a 34972 A LXI Data Acquisition Agilent unit and integrated by LabVIEW version 2017. Five (5) thermocouples were attached on either side of the external wall to measure the outer and inner surface temperatures. Measurements were conducted at  $z = 0.1$  m,  $0.9$  m,  $1.9$  m,  $2.9$  m, and  $3.4$  m. Another five (5) thermocouples were placed on a pole in the cooling chamber  $0.5$  m from the external cold wall to measure  $T_{out}$  at distances  $z = 0.1$  m,  $0.9$  m,  $1.9$  m,  $2.9$  m, and  $3.4$  m. One (1) thermocouple was inserted into the WCJ supply device and another in the outlet air duct to measure  $T_{in}$  and exhaust air temperature, respectively.

## 2.2. Response surface methodology (RSM)

RSM is an aggregate of statistical and mathematical procedures used to design and develop new products, optimize existing product designs, and maximize production [39]. RSM was applied in the design of experiments to develop mathematical models from experimental data. It explained the effect of the four input factors on the two response variables. RSM was incorporated into the study because of its wider application in academic and industrial research [40]. A detailed description of response surface methodology is contained in Ref. [41].

In the current study, RSM was conducted using Minitab version 20.4

(64-bit) 2021. A fractional factorial design based on the Box-Behnken design of the experiment with 25 runs was used instead of the full factorial design for four input factors that required  $3^4 = 81$  runs. The four input factors include  $U_b$ ,  $n$ ,  $T_{in}$ , and  $T_{out}$ . Box-Behnken design entails that factors are transformed from natural to coded variables according to Equation (4) [42].

$$X_i = 2 \frac{x_i - x_{iL}}{x_{iH} - x_{iL}} \quad (4)$$

Where  $X_i$  and  $x_i$  is the  $i$  th factor as coded and natural variables, respectively,  $x_{iL}$ ,  $x_{iM}$  and  $x_{iH}$ , stand for the low, medium, and high levels of each input factor of the  $i$  th natural variable. The coded and actual values of the input parameters are shown in Table 1.

Two analyses were performed to assess the effect of the four input factors on the velocity decay rate and surface temperature on the inner side of the external wall. To predict the rate of velocity decay in the CZ of the WCJ, the slope ( $m$ ) from the regression function that denoted the decay rate of the maximum streamwise velocity ( $U_{max}$ ) was set as the response variable. To estimate the inner wall surface temperature of the external wall ( $T_{wall}$ ), which was weighted by area,  $T_{wall}$  was set as the response variable, while maintaining the same input factors. For each case  $m$  was obtained from the regression function of the line segment from  $z = 0.3$  m to  $z = 2.7$  m.  $T_{wall}$  was measured at five different points on the inner wall surface of the external wall using thermocouples. The actual (measured) values of  $U_b$ ,  $T_{in}$ ,  $T_{out}$ , and  $n$  were the input factors in each analysis.

The relationship between the input factors and  $m$ , and/or  $T_{wall}$  can be described by a general form of the second-order response function of the RSM outlined in Equation (5)

$$y = \beta_0 + \sum_{i=1}^k \beta_i x_i + \sum_{i=1}^k \beta_{ii} x_i^2 + \sum_{ij=1, i \neq j}^k \beta_{ij} x_i x_j + \varepsilon \quad (5)$$

where  $y$  denotes the response variable,  $\beta_0$  is the model constant;  $\beta_i$  is the coefficient of the main term;  $\beta_{ii}$  is the coefficient of the square term;  $\beta_{ij}$  is the coefficient of the interaction term;  $x_i$  and  $x_j$  are the process parameters;  $k$  indicates the number of factors considered and  $\varepsilon$  is a statistical error [42].

## 2.3. Studied cases

A total of Thirty-four (34) cases were studied, namely, nine (9) cases under isothermal and 25 cases under non-isothermal conditions. The design of the experiment matrix under non-isothermal conditions was based on the Box-Behnken design (BBD) [42]. BBD is widely applied in industry and industrial research because it is economical since it requires only a second-order polynomial to be fitted to the three levels (low, medium, and high) for each independent variable (input factor) [39,40]. Isothermal cases were conducted for comparison purposes and were designed by different combinations of the  $U_b$  and  $n$  as shown by runs 26 to 34 in Table 1.  $U_b = 5, 10$ , and  $15$  m/s,  $n = 8, 10$ , and  $12$ .  $T_{in}$

**Table 1**

Coded and actual values of three-level input factors from fractional factorial Response Surface Methodology based on the Box-Behnken design of the experiment.

Non-isothermal cases										
Coded values					Actual values					
Run	$U_b$	$n$	$T_{in}$	$T_{out}$	$U_b$	$n$	$T_{in}$	$T_{out}$	$m$	$T_{wall}$
1	-1	-1	0	0	5.1	8	35.3	0.0	2.1	24.2
2	-1	1	0	0	5.1	12	35.4	0.1	1.1	25.5
3	1	-1	0	0	15.1	8	35.6	1.1	10.3	28.6
4	1	1	0	0	15.0	12	35.5	1.1	10.2	29.1
5	0	0	-1	-1	10.1	10	30.4	-10.1	3.6	22.7
6	0	0	-1	1	10.2	10	30.3	10.1	6.8	26.2
7	0	0	1	-1	10.1	10	40.5	-9.7	2.8	29.4
8	0	0	1	1	10.1	10	40.3	11.1	4.7	33.4
9	-1	0	0	-1	5.0	10	35.0	-10.6	1.1	23.0
10	-1	0	0	1	5.1	10	35.1	9.6	2.1	26.9
11	1	0	0	-1	15.1	10	35.3	-9.1	7.1	27.7
12	1	0	0	1	15.1	10	35.4	10.9	11.5	30.5
13	0	-1	-1	0	10.1	8	30.2	-0.2	6.2	22.8
14	0	-1	1	0	10.1	8	40.2	0.8	4.6	29.9
15	0	1	-1	0	10.0	12	30.6	0.3	3.8	24.6
16	0	1	1	0	10.1	12	40.1	0.9	2.9	32.0
17	-1	0	-1	0	5.0	10	30.2	-0.2	1.1	22.6
18	-1	0	1	0	5.2	10	40.3	0.2	1.3	28.3
19	1	0	-1	0	15.0	10	30.2	0.7	10.5	25.7
20	1	0	1	0	15.1	10	40.3	1.6	8.0	32.6
21	0	-1	0	-1	10.2	8	35.6	-9.5	3.8	25.6
22	0	-1	0	1	10.2	8	35.0	10.4	7.1	28.5
23	0	1	0	-1	10.1	12	35.3	-9.7	2.6	26.9
24	0	1	0	1	10.1	12	35.2	10.3	4.5	29.9
25	0	0	0	0	10.1	10	35.5	-0.1	3.9	27.6
Isothermal cases										
26	-1	-1	-	-	5.2	8	-	-	0.0058	-
27	-1	0	-	-	5.0	10	-	-	0.0049	-
28	-1	1	-	-	5.1	12	-	-	0.0046	-
29	0	-1	-	-	9.9	8	-	-	0.0061	-
30	0	0	-	-	10.2	10	-	-	0.0052	-
31	0	1	-	-	10.1	12	-	-	0.0052	-
32	1	-1	-	-	15.0	8	-	-	0.0062	-
33	1	0	-	-	15.1	10	-	-	0.0056	-
34	1	1	-	-	15.0	12	-	-	0.0061	-

For isothermal cases, [-] for  $T_{in}$  and  $T_{out}$ , indicate an air temperature of about 21 °C.

was the same as  $T_{out}$ . Table 1 shows the coded and actual values for parameters from the design of the experiment with 34 runs with each input factor at (-1, 0, 1), corresponding to (low, medium, and high) levels. Run 25 is the central point of the design of the experiment for non-isothermal conditions.

Depending on the nozzle configuration, the flow rate varied. Table 2 shows the inlet air flow rates for all investigated cases.

Table 2 illustrates that the supply air flow rate increased as  $n$  and  $U_b$  increased.

### 3. Results and discussion

#### 3.1. Flow behavior of WCJ

The velocity and temperature behavior of the WCJ was studied. The characteristic decay factor of  $U_b$  in the streamwise direction is denoted

**Table 2**

Flowrate for investigated cases.

Bulk velocity [m/s]	Number of rows, $n$	Flowrate [m <sup>3</sup> /s]
5	8	0.067
5	10	0.083
5	12	0.296
10	8	0.133
10	10	0.166
10	12	0.199
15	8	0.198
15	10	0.246
15	12	0.296

as  $U^*_{decay}$  (this definition has been also applied in Ref. [19]) for isothermal and non-isothermal cases in all flow regions of the WCJ is shown in Fig. 4. Fig. 4 is a plot of the  $U^*_{decay} = U_b/U_{max}$  against  $z^* = z/d$  where  $U_b$  is inlet bulk velocity,  $U_{max}$  is the maximum streamwise velocity,  $z$  is the distance from the diffuser, and  $d$  is diameter of the nozzle.

Three regions of the isothermal WCJ can be identified: (I) merging region (up to  $z^* < 50$ ); (II) Core zone of WCJ ( $50 < z^* < 500$ ); and (III) impinging zone of the wall region ( $z^* > 500$ ). This means that the merging region occurs in  $z < 0.3$  m, CZ of WCJ is estimated to lie in  $0.3 < z < 3$  m, and the impinging zone  $z > 3.0$  m. The highest  $U^*_{decay}$  occurs

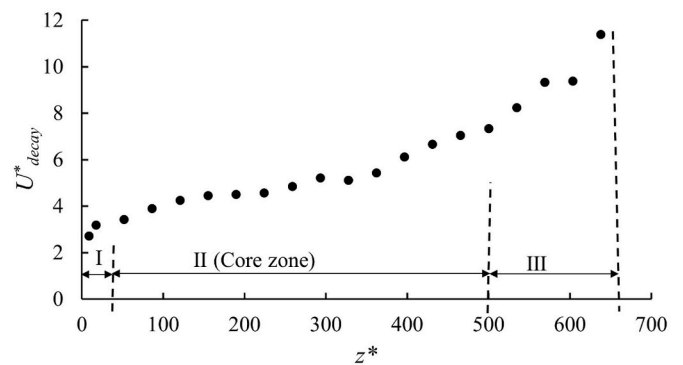


**Fig. 4.** Illustration of the velocity decay in the various flow regions: Region (I) is the merging region, (II) is the wall confluent core zone (III) is the impinging zone of the wall region; where;  $U^*_{decay} = U_b/U_{max}$ ;  $z^* = z/d$ .

in the merging region caused by the resultant flow behavior due to low-pressure regions between the individual jets. Individual jets merge into a single bigger jet in this flow region. The lowest  $U^*_{\text{decay}}$  occurs in the CZ. The wall-impinging region occurs closer to the floor has also high  $U^*_{\text{decay}}$  similar to the merging region. The current study focuses on the CZ and only analyses of the velocity and temperature behavior of the CZ are presented in the following sections.

Fig. 5 is a representative plot to show how varying supply air velocity affects the  $U^*_{\text{decay}}$ . While keeping the remaining three parameters constant at  $n = 10$ ,  $T_{\text{in}} = 30^\circ\text{C}$ , and  $T_{\text{out}} = 0^\circ\text{C}$  for non-isothermal cases. For isothermal cases:  $n = 10$ ,  $T_{\text{in}} = 21^\circ\text{C}$  and  $T_{\text{out}} = 21^\circ\text{C}$ .

The shape of dimensionless velocity profiles is similar for all the bulk velocities under isothermal and non-isothermal conditions. The  $U^*_{\text{decay}}$  is higher as  $U_b$  increases under both isothermal and non-isothermal conditions. Higher velocity decay rates are observed under non-isothermal conditions than under isothermal conditions. This is due to buoyancy effects. The current study considered a confined WCJ due to the restrictions imposed by the cold wall and the floor. In a confined wall jet, wall friction from the cold wall contributes to the magnitude of the  $U^*_{\text{decay}}$ . On the other hand, the floor seems to exert a compressive force on the jet, especially for high-velocity jets. The floor acts as an obstacle to the high-velocity jet, thus the jet impinges while still retaining sufficient momentum. This contributes to faster decay rates for higher  $U_b$ . Due to physical space constraints in the laboratory, the effect of the inlet air discharge height was not in focus in the study. The effect of the discharge height on the flow and thermal behavior of the WCJ requires further investigation. Numerical studies using computational fluid dynamics (CFD) are planned to assess the effect of discharge height on the flow behavior of the WCJ.

The effect of  $n$  on the  $U^*_{\text{decay}}$  is shown in Fig. 6. Fig. 6 is a representative plot to illustrate how the size of the nozzle array affects the decay factor of  $U_b$ . The  $U_b$ ,  $T_{\text{in}}$ , and  $T_{\text{out}}$  are kept constant at 10 m/s,  $35^\circ\text{C}$ , and  $10^\circ\text{C}$ , respectively while  $n$  is varied.

The  $U^*_{\text{decay}}$  is higher at a lower  $n$  for both isothermal and non-isothermal conditions. This is attributed to the reduced shielding effect as the number of nozzles becomes smaller. Larger nozzle arrays provide better shielding of the jet far downstream which reduces the entrainment of the ambient room air.

The effects of  $T_{\text{in}}$  and  $T_{\text{out}}$  are analyzed in Fig. 7. Fig. 7 is a representative plot to illustrate how  $T_{\text{in}}$  and  $T_{\text{out}}$  influence the  $U^*_{\text{decay}}$ .  $U_b$  and  $n$  are kept constant at 10 m/s and 10 respectively, while  $T_{\text{in}}$  and  $T_{\text{out}}$  varied.

At a given  $U_b$  and  $n$ , the  $U^*_{\text{decay}}$  was higher as  $T_{\text{in}}$  and  $T_{\text{out}}$  decrease. This is attributed to enhanced convection caused by the temperature difference between  $T_{\text{in}}$  and  $T_{\text{out}}$  which increases as the  $T_{\text{out}}$  decreases. This effect was also observed, where the  $U^*_{\text{decay}}$  was higher under non-

isothermal than under isothermal conditions. This is due to buoyancy effects that make the less dense warm jet ineffective in overcoming the fluid resistance caused by the denser cool room air. The advection effects of the warm jet increase mixing with room air which increases entrainment and reduces jet momentum.

The flow behavior of WCJ in the CZ is demonstrated by dimensionless velocity profiles at  $z = 1.3$  m for both isothermal and non-isothermal conditions presented in Fig. 8. Fig. 8 is a plot of  $U^*$  vs  $x^*$ , where  $U^* = U/U_{\text{max}}$  and  $x^* = x/x_{0.5}$ , where  $U$  is the local velocity,  $U_{\text{max}}$  is the streamwise maximum velocity,  $x$  is the distance from the external cold wall's inner surface towards the center of the room, and  $x_{0.5}$  is the point at which  $U_{\text{max}}$  is halved.

The dimensionless velocity profile shape is similar under all values of  $U_b$  under isothermal and non-isothermal conditions. Fig. 8 confirms the jet attached to the wall due to the Coanda effect and that the  $U_{\text{max}}$  position is closer to the external cold wall for points nearer the inlet diffuser. The flow behavior of WCJ in the core zone is further analyzed using dimensionless velocity profiles for Run 25 at selected points between  $z = 0.3$  m and  $z = 2.7$  m as shown in Fig. 9.

Fig. 9 shows that the WCJ has attached to the wall and remains attached as it propagates toward the floor. The shape of the dimensionless velocity profile remains the same as the WCJ propagates toward the floor. The dimensionless velocity profiles for successive points ( $z = 0.5$  m to  $z = 1.3$  m); ( $z = 1.7$  m to  $z = 2.1$  m) and ( $z = 2.3$  m to  $z = 2.7$  m) are similar which indicates low rates of  $U_{\text{max}}$  decay in the CZ. However, the velocity profiles slightly differ for points located nearer to the inlet air diffuser, i.e.,  $z = 0.5$  m from those closer to the floor,  $z = 2.7$  m. This is because the lateral spread of the jet increases while  $U_{\text{max}}$  decreases far downstream. The overheated WCJ along the cold wall slows down due to the fluid resistance of the denser and lower-temperature stagnant room air. The variance in the temperature of the wall, WCJ, and room air increases the diffusivity of the jet. The increase in diffusivity of the jet increases the wall friction which causes  $U_{\text{max}}$  to decay faster. Like any other wall-bounded jet, turbulence is expected and attributed to a high exchange of momentum within the boundary layer. In addition, the momentum of the jet decreases as the distance from the inlet air diffuser increases due to wall friction. The combined effect of jet momentum and thermal variations in the room enhances forced convection, which increases the mixing of the jet and room air. As the jet entrains room air, it loses its momentum and increases in thickness. Closer to the floor, the jet almost flattens with the maximum velocity located away from the cold wall but is still attached to the wall. This could be attributed to the characteristic turbulent flow behavior which delays the separation of flow in the boundary layer proximal to the wall. Notwithstanding the effect of the wall and floor, the pattern of the dimensionless velocity profiles is similar to those in the primary region of the WCJ observed by

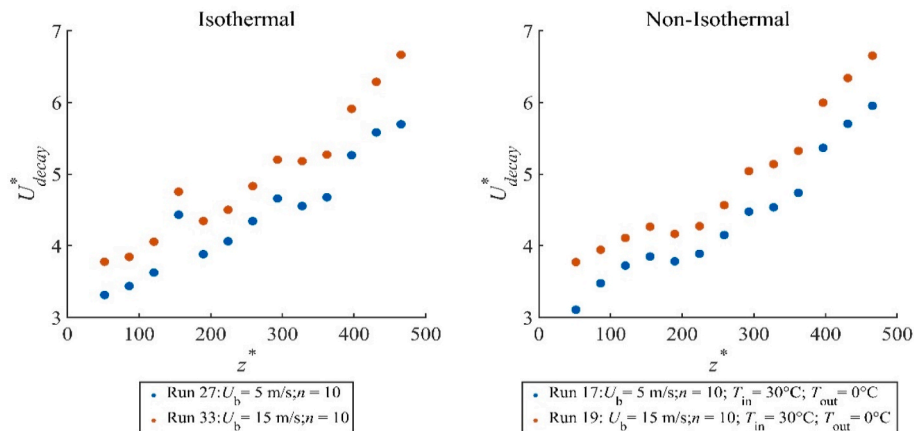
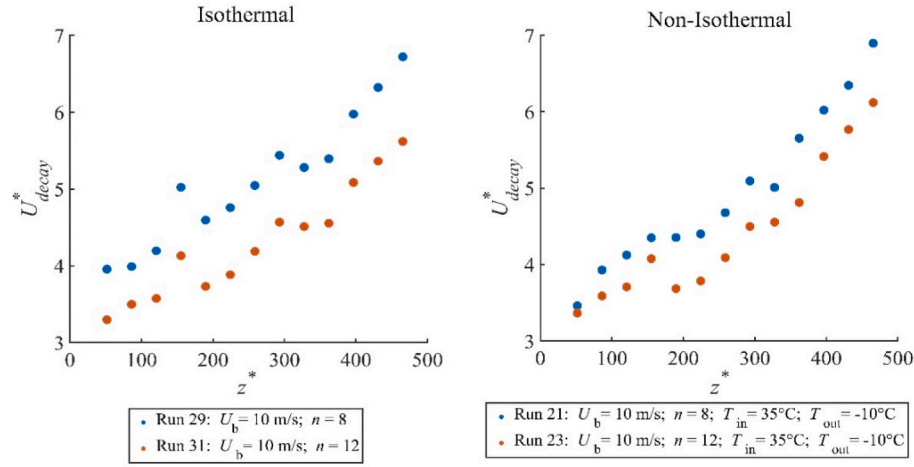
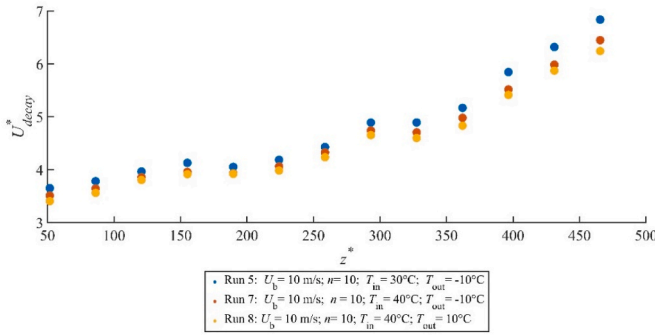


Fig. 5. Dimensionless velocity decay profiles for isothermal and non-isothermal conditions to illustrate the effect of  $U_b$  on the  $U^*_{\text{decay}}$ , where;  $U^*_{\text{decay}} = U_b/U_{\text{max}}$   $z^* = z/d$ .



**Fig. 6.** Effect of the number of nozzles on the  $U^*_{\text{decay}}$  in the core zone of WCJ, where;  $U^*_{\text{decay}} = U_b/U_{\text{max}}$   $z^* = z/d$ .



**Fig. 7.** Effect of the inlet air temperature and outdoor air temperature on the  $U^*_{\text{decay}}$  in the core zone where;  $U^*_{\text{decay}} = U_b/U_{\text{max}}$   $z^* = z/d$ .

Ref. [27].

### 3.2. Temperature and thermal behavior of WCJ

The temperature of the WCJ in the CZ is represented by the dimensionless temperature profiles shown in Fig. 9 for  $z = 1.3$  m. Fig. 10 is a representative plot of  $T^*_{\text{WCJ}}$  against  $x^*$ , where  $T^*_{\text{WCJ}} = \frac{(T_{\text{WCJ}} - T_{\text{out}})}{(T_{\text{in}} - T_{\text{out}})}$ ,  $x^* = x/x_{0.5}$ .  $T_{\text{WCJ}}$  is the air jet local temperature.

Fig. 10 shows that the dimensionless temperature profiles are similar for all bulk velocities, but the magnitude of the profiles increases with an increase in inlet bulk velocity. This indicates that a high-velocity WCJ is hotter and can heat the cold wall better than a lower-velocity jet. This shows that a warm boundary layer of WCJ forms on the cold wall which acts as “insulation” on the cold wall. This characteristic flow behavior can allow the WCJ to heat the inner surfaces of the external wall in large-space enclosures. This can prevent cold drafts through such facades in cold periods, without altering the aesthetic properties or blocking

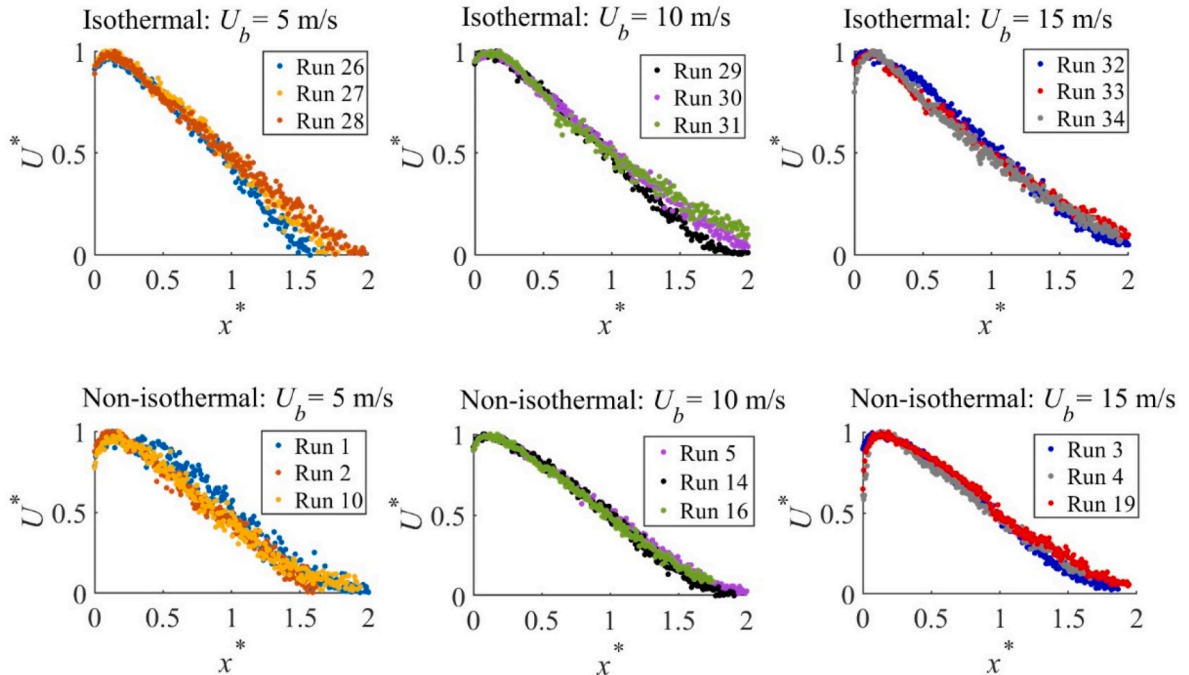


**Fig. 8.** Dimensionless velocity profiles at  $z = 1.3$  m in the core zone of the WCJ region under isothermal and non-isothermal conditions.  $U^* = U/U_{\text{max}}$   $x^* = x/x_{0.5}$ .



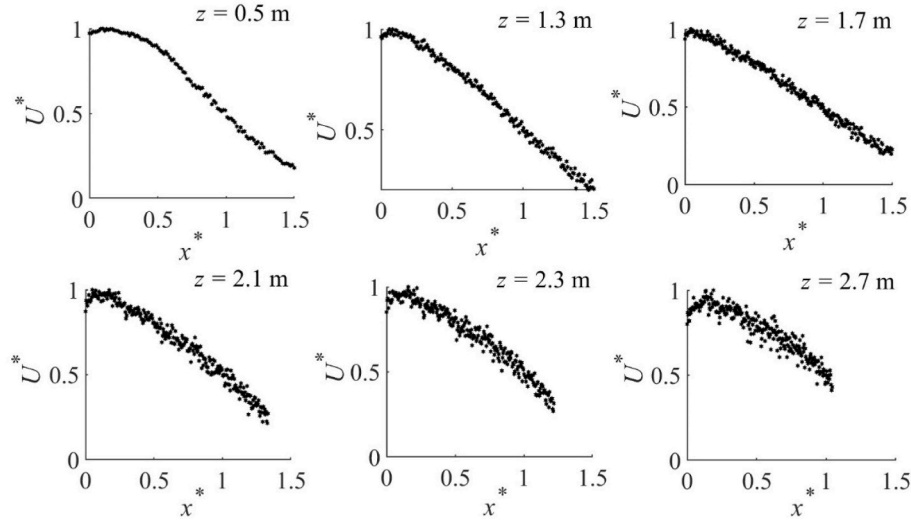


Fig. 9. Dimensionless velocity profiles at selected points in the core zone of WCJ for Run 25. Note:  $U^* = U/U_{max}$ ,  $x^* = x/x_{0.5}$ .

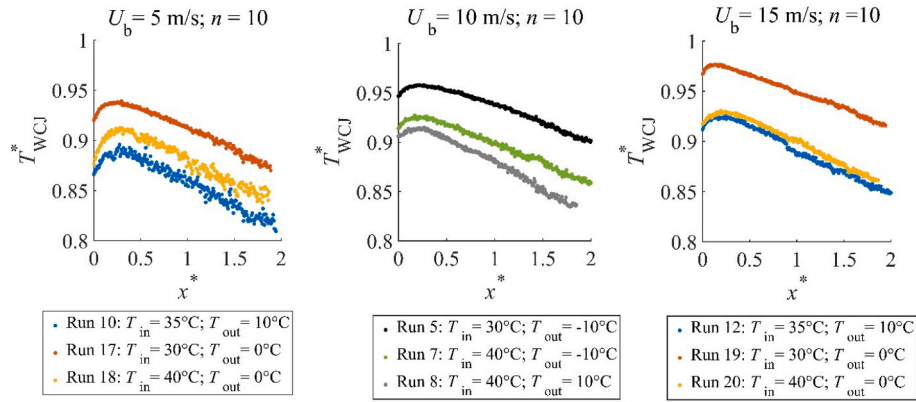


Fig. 10. Dimensionless inner surface temperature of the external wall at  $z = 1.3$  m,  $T_{WCJ}^* = \left( \frac{T_{WCJ} - T_{out}}{T_{in} - T_{out}} \right)$ , representing how the WCJ will insulate the wall at the three bulk velocities.  $x^* = x/x_{0.5}$ .

sunlight. Additionally, the mixing of the jet and room air increases the temperature of the room air, thereby affecting the indoor thermal environment. The dimensionless temperature profiles are higher for lower  $T_{in}$  and  $T_{out}$  because of the smaller temperature difference which inhibits large heat transfer from the jet to the wall. The WCJ retains much of its heat when supplied at a lower temperature.

The wall heating effect of the WCJ is analyzed in Fig. 11. Fig. 11 is a

representative plot of the dimensionless temperature profile,  $T_w^*$  against  $z^*$ ; where,  $T_w^* = \left( \frac{T_{wall} - T_{out}}{T_{in} - T_{out}} \right)$  vs.  $z^* = z/d$ ,  $T_{wall}$  is the local surface temperature of the cold wall.

Fig. 11 indicates that the wall heating effect of the WCJ increases with an increase in  $U_b$ . This is attributed to the turbulent flow behavior, which is expected as a high-momentum warmer wall jet flows into a

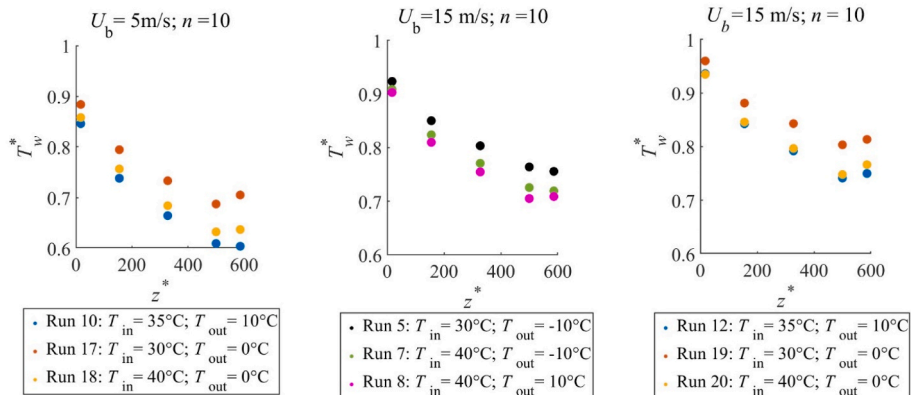


Fig. 11. Wall heating effect of the WCJ at the five points along the wall for the three inlet bulk velocities,  $T_w^* = \left( \frac{T_{wall} - T_{out}}{T_{in} - T_{out}} \right)$  and;  $z^* = z/d$ .

room with stagnant cooler air, thereby enhancing heat transfer to the cold wall. A turbulent warm air-cold wall boundary layer boosts the shear stress which increases the drag force on the cold wall. No-slip conditions and high fluid resistance at the cold wall surface improve heat transfer from the jet to the cold wall by increasing the residence time of the warm air. Increased fluid shear and buoyancy effects of higher momentum WCJ cause an increase in the jet's turbulent kinetic energy. Dissipation of the turbulent kinetic energy increases the internal energy of the jet which raises the temperature of both the jet and the wall as the energy dissipates. The wall heating effect of the WCJ reduces as the  $T_{out}$  increases. The heating of the wall surfaces by WCJ is enhanced by convective heat transfer from the jet to the cold wall. This is attributed to reduced heat transfer across the cold wall due to the smaller temperature difference between the internal and external wall surface temperatures. Due to the rather low supply of air temperature, one can incorporate industrial waste heat into the WCJ heating systems. This integration would reduce not only the exergy for the heating demand but also result in a cost-effective and environmentally friendly heating system for large-space enclosures.

### 3.3. Regression analysis in the core zone

Regression analysis was performed for the segment  $z = 0.3$  m to  $z = 2.7$  m in the CZ of the WCJ to determine the  $U^*_{decay}$ . Wall friction, momentum, and buoyancy forces influence the flow patterns of the WCJ along the cold wall. Buoyancy forces exist due to air density differences caused by temperature differences between the WCJ and the room air. Buoyancy forces affect the jet's trajectory, the throw of the jet, and the point of attachment to the wall [43]. Several earlier studies used the Archimedes number (Ar) to evaluate the effect of buoyancy and momentum forces on the air jet [43,44]. The current study employed the Ar to explore the buoyancy effects on the WCJ. Equation (6) describes the Ar used to analyze the effects of thermal variations on the WCJ.

$$Ar = \frac{g\beta d_s(T_{in} - T_{out})}{U_b^2} \quad (6)$$

Where;  $g$  is gravitational acceleration,  $\beta = \frac{1}{\left(\frac{T_{in} + T_{out}}{2}\right)}$ ,  $d_s$  is effective source diameter based on the number of nozzles, i.e., for nozzle arrays:  $8 \times 62$ ,  $d_s = 0.129$  m;  $10 \times 62$ ,  $d_s = 0.146$  m, and  $12 \times 62$ ,  $d_s = 0.158$  m.

The regression equation is a linear function of the form given in Equation (7) [27].

$$U^*_{decay} = mAr\left(\frac{z}{d}\right) + c \quad (7)$$

Where  $U_b$  is inlet bulk velocity,  $U_{max}$  is the local maximum velocity,  $m$  is the slope of the regression line,  $Ar$  is Archimedes number,  $z$  is the distance from the inlet air diffuser,  $d$  is the diameter of the nozzle and  $c$  is the y-intercept of the regression line.

The natural logarithm of  $m$  is plotted against the  $Ar$  in Fig. 12. Fig. 12 shows the investigated non-isothermal cases classified based on  $Ar$  and the natural logarithm of  $m$ .

Fig. 12 shows that the  $m$  increases with an increase in the  $U_b$  while the  $Ar$  reduces with an increase in  $U_b$ . The increase in  $m$  with an increase in  $U_b$  indicates that the  $U^*_{decay}$  is higher when the momentum of the jet increases. Based on the magnitude of  $Ar$ , cases are divided into two groups: the first group contains cases with  $Ar$  less than 0.004 which belong to  $U_b$  of 10 m/s and 15 m/s. The second group has cases with  $Ar$  greater than 0.004 for  $U_b$  of 5 m/s. The average slope was 1.46, 4.40, and 9.61 for all cases with  $U_b = 5$  m/s, 10 m/s, and 15 m/s, respectively. The regression functions for the line segment of  $z = 0.3$  m to  $z = 2.7$  m for  $U_b = 5$  m/s, 10 m/s, and 15 m/s are given by Equations (8)–(10), respectively. The average  $R^2$ -values in Equations (8)–(10), are 90.5%, 91.2%, and 91.3%, respectively.

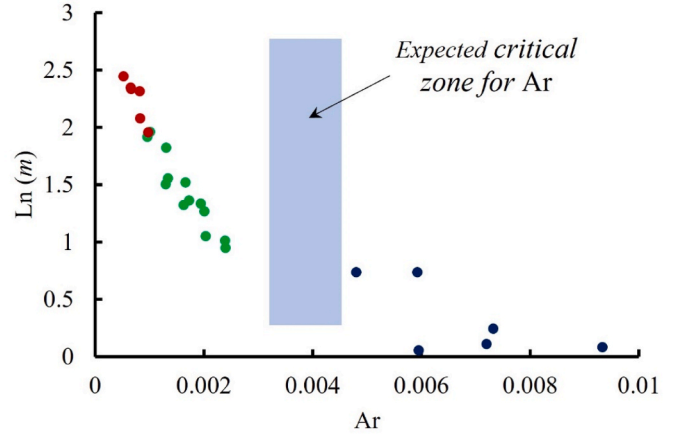


Fig. 12. Natural logarithmic  $m$  from regression line vs  $Ar$  for segment  $z = 0.3$  m to  $z = 2.7$  m in the CZ of the WCJ. Dark blue dots represent  $U_b = 5$  m/s, green dots represent  $U_b = 10$  m/s, and red dots represent  $U_b = 15$  m/s. (For interpretation of the references to colour in this figure legend, the reader is referred to the Web version of this article.)

$$U^*_{decay} = 1.46 \left( Ar \times \frac{z}{d} \right) + 2.48 \quad (8)$$

$$U^*_{decay} = 4.40 \left( Ar \times \frac{z}{d} \right) + 2.95 \quad (9)$$

$$U^*_{decay} = 9.61 \left( Ar \times \frac{z}{d} \right) + 3.11 \quad (10)$$

A critical  $Ar$  exists in the zone  $0.0025 < Ar < 4.5$  at which the  $m$  changes abruptly between the higher and lower  $U_b$  of the WCJ. This requires further investigation. This flow behavior is attributed to an increase in turbulence and buoyancy as the velocity of the jet increases. The extent of the CZ was undetermined because the effect of the floor on the jet was unquantified. Computational studies are planned to determine the extent of the CZ of the WCJ. However, this study could be used as a basis for validation for future computational studies on the length of the CZ. Comparing  $m$  for the same segment between isothermal and non-isothermal conditions by using Equation (7), without incorporating the  $Ar$  gives  $m$  of 0.0051, 0.0055, and 0.0060 for  $U_b = 5$  m/s, 10 m/s, and 15 m/s, respectively under isothermal conditions. Under non-isothermal conditions,  $U_b = 5$  m/s, 10 m/s, and 15 m/s had  $m$  of 0.0094, 0.0067, and 0.0069, respectively. Thus,  $m$  is higher under non-isothermal than isothermal conditions. The value of  $m$  for  $U_b = 5$  m/s was the highest under non-isothermal conditions which could be attributed to the effect of the floor on the jet. The jet could have lost most of its momentum, resulting in a faster decay of  $m$  at  $z = 2.7$  m.

### 3.4. Response surface methodology (RSM) analysis for velocity and temperature

The effect of all four parameters on the decay of  $U_{max}$  was analyzed simultaneously using RSM. Results show that all linear terms ( $U_b$ ,  $n$ ,  $T_{in}$ , and  $T_{out}$ ), one quadratic term ( $U_b \times U_b$ ), and two-way interacting factors ( $U_b \times T_{in}$  and  $U_b \times T_{out}$ ) had a critical effect on the  $m$ . The  $U_b$  had the highest effect, and the two-way interaction ( $U_b \times T_{in}$ ) had the least influence among the critical factors. The order of the independent parameters' effect on the  $m$  starting with the strongest is given as follows:  $U_b$ ,  $T_{out}$ ,  $n$ ,  $T_{in}$ ,  $U_b \times U_b$ ,  $U_b \times T_{out}$ , and  $U_b \times T_{in}$ . The effect of  $U_b$  on the slope is nine times that of  $U_b \times T_{in}$ . This confirms the result of a previous study that found that non-isothermal WCJ is more sensitive to inlet air velocity [45].

The effect of the input factors on the temperature of the external wall surface ( $T_{wall}$ ) was also analyzed by RSM. The measured inner surface

temperature of the external wall ( $T_{\text{wall}}$ ) which was weighted by area was set as the *response* variable. To illustrate how accurate the Response surface (RS) models were, a plot of the  $m$  from regression analysis ( $m_{\text{regression}}$ ) and  $m$  predicted by Minitab ( $m_{\text{RSM predicted}}$ ) were plotted against each other as shown in Fig. 13 (a). Fig. 13 (b) shows a plot of the measured weighted inner wall surface temperature ( $T_{\text{wall measured}}$ ) vs. the RSM predicted inner surface temperature ( $T_{\text{wall RSM predicted}}$ ).

The good agreement between the  $m_{\text{regression}}$  and  $m_{\text{RSM predicted}}$  shows that the RS model for velocity decay analysis had high accuracy. The RSM model had a high performance as indicated by a higher coefficient of determination ( $R^2$ -value) of 99.0%. High  $R^2$  illustrates that the quadratic model efficiently fitted the experimental data of the independent factors to give an accurate RS model of the slope. The RS model performance had an adjusted  $R^2$  value of 97.6%. This indicates that there was a good agreement between  $m_{\text{regression}}$  and  $m_{\text{RSM predicted}}$ .

The RS model for the  $T_{\text{wall}}$  analysis had  $R^2$ -value of 99.3% and an adjusted  $R^2$ -value of 98.3%. Table 3 contains coefficients for the second-order polynomial fitted in the RS model equations for  $m$  and  $T_{\text{wall}}$ . Only the linear terms had a critical effect on  $T_{\text{wall}}$ .  $T_{\text{in}}$  had the highest effect ( $T_{\text{in}}$  about three times the effect of  $n$ ) while  $n$  had the least effect. The quadratic and two-way interacting terms contributed minimally to  $T_{\text{wall}}$ .

The second-order polynomial fitted for the RS model for  $m$  is given by Equation (11)

$$m = 21.1 + 0.518 U_b - 3.37 n - 0.153 T_{\text{in}} + 0.340 T_{\text{out}} + 0.0518 U_b \times U_b + 0.1065 n \times n + 0.0016 T_{\text{in}} \times T_{\text{in}} + 0.00214 T_{\text{out}} \times T_{\text{out}} + 0.0231 U_b \times n - 0.02828 U_b \times T_{\text{in}} + 0.01724 U_b \times T_{\text{out}} + 0.0184 n \times T_{\text{in}} - 0.0149 n \times T_{\text{out}} - 0.00674 T_{\text{in}} \times T_{\text{out}} \quad (11)$$

The RS model equation for the fitted second-order polynomial to approximate  $T_{\text{wall}}$  is given Equation (12)

$$T_{\text{wall}} = 2.4 + 0.504 U_b + 1.23 n + 0.054 T_{\text{in}} + 0.168 T_{\text{out}} - 0.02128 U_b \times U_b - 0.0601 n \times n + 0.00526 T_{\text{in}} \times T_{\text{in}} + 0.00235 T_{\text{out}} \times T_{\text{out}} - 0.0115 U_b \times n + 0.01145 U_b \times T_{\text{in}} - 0.00559 U_b \times T_{\text{out}} + 0.0127 n \times T_{\text{in}} - 0.0015 n \times T_{\text{out}} + 0.00204 T_{\text{in}} \times T_{\text{out}} \quad (12)$$

Equations (11) and (12) are correlations that can be used to determine  $m$  and  $T_{\text{wall}}$  in the CZ of WCJ from any given values of the input factors. The effect of any two parameters on  $m$  while keeping the other two factors constant at their medium-value level is shown by the contour plots in Fig. 14 (a)–(f).

Fig. 14 (a) shows that  $m$  increases as the  $U_b$  increases while the  $n$  decreases. Fig. 14 (b) indicates that the  $m$  is higher at lower  $T_{\text{in}}$  and higher  $U_b$ . Fig. 14 (c) illustrates that the  $m$  increases as  $T_{\text{out}}$  and  $U_b$  increase. Fig. 14 (d) shows that the  $m$  increases as the  $T_{\text{in}}$  and the  $n$  decrease. This is attributed to the lower temperature difference between

**Table 3**

Coefficients of the second-order polynomial for the RS models for  $m$  and  $T_{\text{wall}}$ .

Source	RS Coefficients for $m$ model	P-Value	RS Coefficients for $T_{\text{wall}}$ model	P-Value
Constant	21.10		2.4	
Linear terms				
$U_b$	0.52	0.00	0.50	0.00
$n$	-3.37	0.00	1.23	0.00
$T_{\text{in}}$	-0.15	0.00	0.05	0.00
$T_{\text{out}}$	0.34	0.00	0.17	0.00
Quadratic terms				
$U_b \times U_b$	0.052	0.00	-0.02	0.05
$n \times n$	0.11	0.19	-0.06	0.36
$T_{\text{in}} \times T_{\text{in}}$	0.00	0.89	0.01	0.60
$T_{\text{in}} \times T_{\text{out}}$	0.00	0.48	0.00	0.34
$T_{\text{out}} \times T_{\text{out}}$				
Two-Way Interacting terms				
$U_b \times n$	0.02	0.38	-0.01	0.59
$U_b \times T_{\text{in}}$	-0.03	0.02	0.01	0.19
$T_{\text{in}} \times T_{\text{out}}$				
$U_b \times T_{\text{out}}$	0.02	0.01	-0.01	0.20
$n \times T_{\text{in}}$	0.02	0.49	0.01	0.56
$n \times T_{\text{out}}$	-0.02	0.26	-0.00	0.89
$T_{\text{in}} \times T_{\text{out}}$	-0.01	0.20	0.00	0.62
$T_{\text{out}} \times T_{\text{out}}$				

The RS models established how the parameters affected the  $m$  and  $T_{\text{wall}}$ . The probability values (P-values) were used as the basis to ascertain the significance of each coefficient. In the present study P-values < 0.05 indicate that factors have a significant effect on the  $m$  and  $T_{\text{wall}}$ .

the WCJ temperature and ambient air temperature. Fig. 14 (e) indicates that  $m$  increases as the  $T_{\text{out}}$  increases at a lower  $n$ . The shielding effect of the nozzle array configuration reduces as the  $n$  decreases. This causes faster decay of maximum velocity. Fig. 14 (f) shows that the  $m$  is higher at higher  $T_{\text{out}}$  and lower  $T_{\text{in}}$ . The  $m$  is highest in conditions of higher  $U_b$  and  $T_{\text{out}}$ .  $U_{\text{max}}$  decays faster due to enhanced mixing and entrainment of room air caused by momentum and buoyancy variations between the jet and the ambient.

The effect of any two parameters on  $T_{\text{wall}}$  while keeping the other two factors constant at their medium-value level is shown by the contour plots in Fig. 15 (a)–(f).

Fig. 15 (a) indicates that  $T_{\text{wall}}$  increases as  $n$  and  $U_b$  increase.  $U_b$  has a stronger influence than  $n$  in this interaction. The WCJ retains a higher temperature downstream due to the shielding effect of the larger-nozzle arrays as  $n$  increases. Fig. 15 (b) shows that  $T_{\text{wall}}$  increases as the  $T_{\text{in}}$  and  $U_b$  increase.  $T_{\text{in}}$  has a stronger influence than  $U_b$ . Fig. 15 (c) illustrates

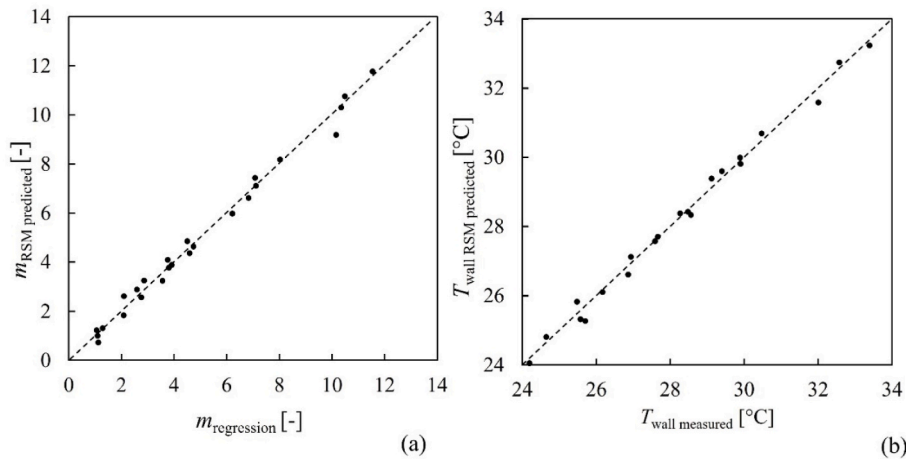


**Fig. 13.** Slope from regression analysis ( $m_{\text{regression}}$ ) vs. predicted slope generated by RSM ( $m_{\text{RSM predicted}}$ ) in Minitab for the final RS Model. The 45° straight line demonstrates a perfect fit.

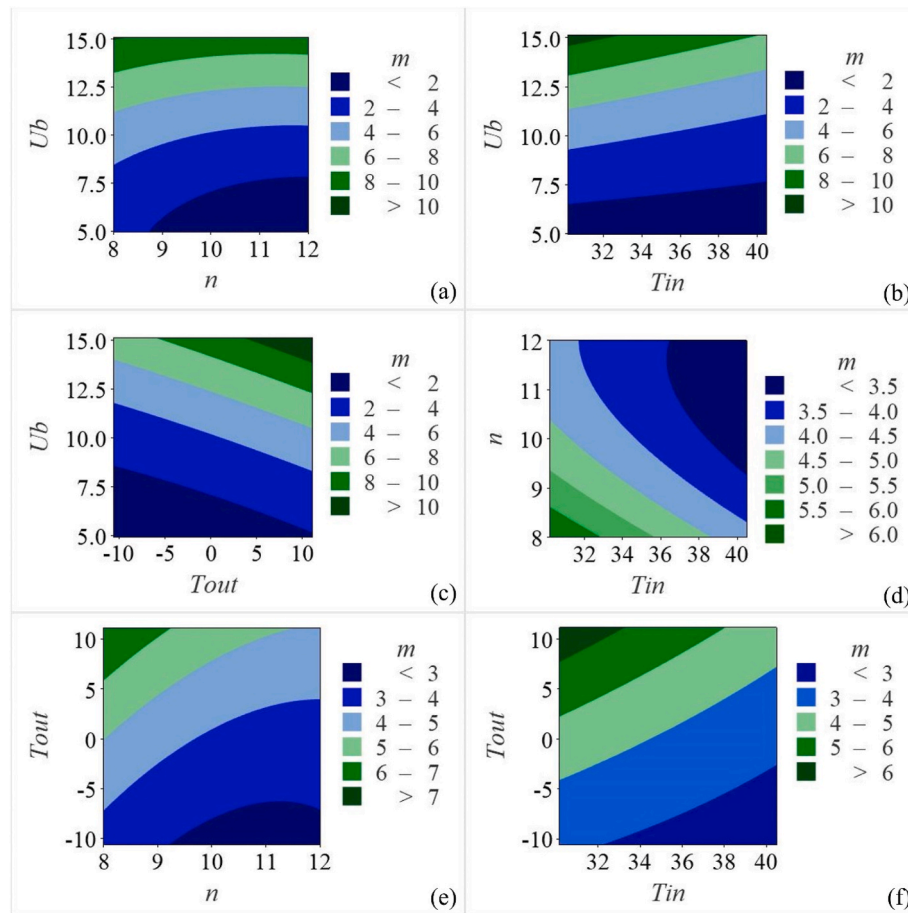


Fig. 14. Effect of input factors on the decay rate ( $m$ ) of maximum streamwise velocity ( $U_{max}$ ).

that  $T_{wall}$  increases as  $T_{out}$  and  $U_b$  increase. Fig. 15 (d) shows that  $T_{wall}$  increases as  $T_{in}$  and  $n$  increase. Fig. 15 (e) demonstrates that  $T_{wall}$  increases with an increase in  $T_{out}$  and  $n$ . Fig. 15 (f) shows that the  $T_{wall}$  increases as  $T_{in}$  and  $T_{out}$  increase. This is attributed to less heat transfer through the wall due to the low-temperature difference between the WCJ jet temperature and  $T_{out}$ . Fig. 15(b), (d), and (f) show higher  $T_{wall}$  due to the stronger effect of the  $T_{in}$  in the interactions.

In summary, RSM revealed how each parameter influenced the decay rate of the maximum velocity and the temperature on the inner surface of the external wall. Of all the critical parameters,  $U_b$  had the strongest effect on  $m$  and was nine times greater than the effect of the two-way interaction between  $U_b \times T_{in}$ .  $T_{in}$  had the highest impact on  $T_{wall}$  and was three times stronger than the effect of  $n$ . Correlations which are second-order polynomial equations to estimate  $m$  and  $T_{wall}$  in the CZ of the WCJ were obtained.

Future works will involve several computational studies to investigate in greater detail the flow and thermal characteristics of WCJ. More experimental studies are planned, and others are already taking place at a field greenhouse site to understand the ability of the WCJ to provide an optimum crop-growing environment in a real environment. Other studies will assess how regional energy systems (excess industrial waste heat) can be harnessed and incorporated into the confluent jet technology to heat greenhouse premises. Numerical studies using computational fluid dynamics (CFD) are planned to assess the effect of discharge height on the flow behavior of the WCJ in the CZ.

#### 4. Conclusions

The flow and temperature behavior in the CZ of WCJ propagating along an external cold wall of large-space enclosures such as a

greenhouse was investigated. The effect of the inlet bulk velocity, the number of nozzles, inlet air temperature, and outdoor air temperature on the  $U^*_{decay}$  in the CZ was explored. The results show that the WCJ attached to the wall as it propagated towards the floor under both isothermal and non-isothermal conditions. This flow behavior suggests that the WCJ can be used to heat the glass facades of large-space enclosures. The  $U^*_{decay}$  was higher under non-isothermal than under isothermal conditions in the CZ. The inlet bulk velocity had the highest effect on the  $U^*_{decay}$  and it increased with the increase in inlet bulk velocity. The inlet air temperature affected the  $U^*_{decay}$  the least. The  $U^*_{decay}$  increased as the number of nozzles decreased. The  $U^*_{decay}$  was higher at lower inlet air temperatures and outdoor air temperatures. The  $U^*_{decay}$  was higher at higher  $U_b$ , higher  $T_{out}$ , lower  $n$ , and lower  $T_{in}$ .

It was observed that a high-momentum jet with a higher inlet air temperature will insulate the external cold wall effectively.  $T_{in}$  had the highest effect on  $T_{wall}$  while  $n$  had the least effect. Correlations of the second-order polynomials fitted for the RS models that can be used to calculate  $m$  and  $T_{wall}$  were obtained.

#### Funding

This work was supported by the Swedish Agency for Economic and Regional Growth through the European Regional Development Fund (ERDF).

#### CRediT authorship contribution statement

**Gasper Choonya:** Writing – original draft, Validation, Software, Methodology, Investigation, Formal analysis, Data curation, Conceptualization. **Ulf Larsson:** Writing – review & editing, Validation,



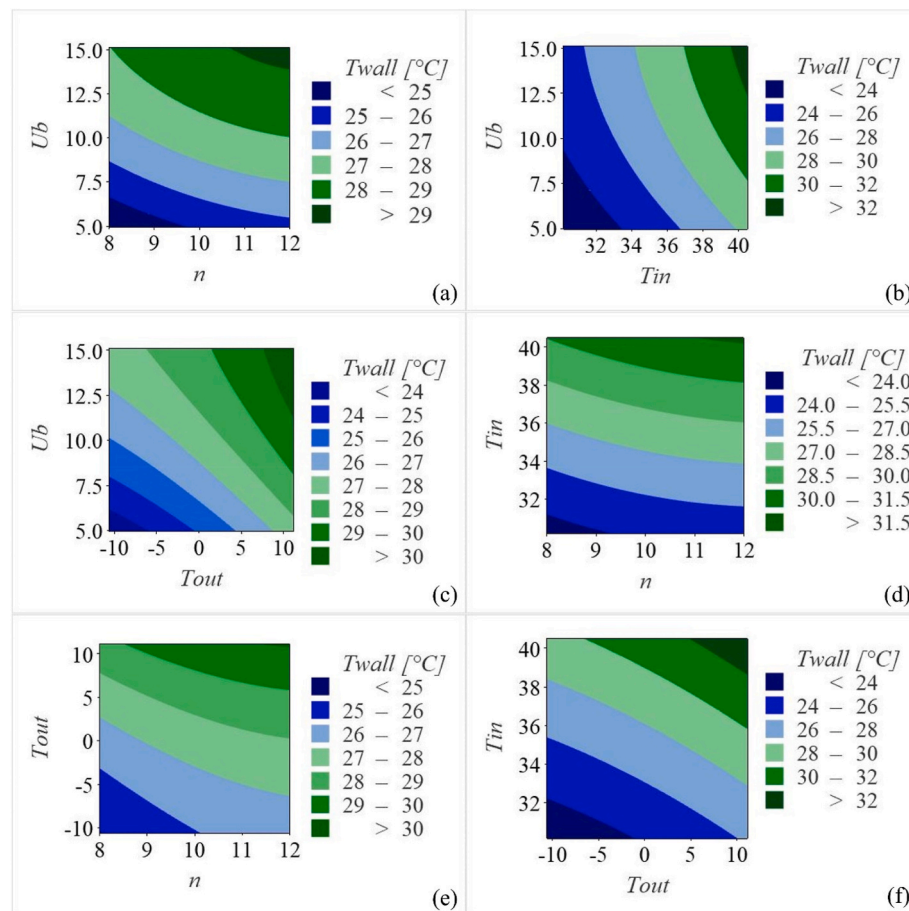


Fig. 15. Influence of parameters on the temperature of the inner surface ( $T_{wall}$ ) of the PVC wall.

Supervision, Resources, Project administration, Methodology, Funding acquisition, Conceptualization. **Bahram Moshfegh**: Writing – review & editing, Validation, Supervision, Resources, Project administration, Methodology, Funding acquisition, Formal analysis.

#### Declaration of competing interest

The authors declare the following financial interests/personal relationships which may be considered as potential competing interests:

Prof. Bahram Moshfegh reports financial support was provided by Swedish Agency for Economic and Regional Growth.

#### Data availability

Data will be made available on request.

#### Acknowledgments

The authors gratefully acknowledge technical support from the staff at the University of Gävle laboratory including Ms. Elisabet Linden, Mr. Rikard Larsson, Mr. Ula Jeppison, Mr. Mikael Sundberg, Mr. Hans Lundström, and Mr. Getiye Woodaje Gebeyew.

#### References

- [1] U. Soytaş, R. Sari, Energy consumption, economic growth, and carbon emissions: challenges faced by an EU candidate member, *Ecol. Econ.* 68 (6) (2009) 1667–1675, <https://doi.org/10.1016/j.ecolecon.2007.06.014>.
- [2] D. Ürge-Vorsatz, A. Novikova, S. Köppel, B. Boza-Kiss, Bottom-up assessment of potentials and costs of CO<sub>2</sub> emission mitigation in the buildings sector: insights into the missing elements, *Energy Effic* 2 (4) (2009) 293–316, <https://doi.org/10.1007/s12053-009-9051-0>.
- [3] D. Urge-Vorsatz, K. Petrichenko, M. Staniec, J. Eom, Energy use in buildings in a long-term perspective, *Curr. Opin. Environ. Sustain.* 5 (2) (2013) 141–151.
- [4] L. Pérez-Lombard, J. Ortiz, J.F. Coronel, I.R. Maestre, A review of HVAC systems requirements in building energy regulations, *Energy Build.* 43 (2–3) (2011) 255–268, <https://doi.org/10.1016/j.enbuild.2010.10.025>.
- [5] L. Pérez-Lombard, J. Ortiz, C. Pout, A review on buildings energy consumption information, *Energy Build.* 40 (3) (2008) 394–398, <https://doi.org/10.1016/j.enbuild.2007.03.007>.
- [6] L. Yang, H. Yan, J.C. Lam, Thermal comfort and building energy consumption implications - a review, *Appl. Energy* 115 (2014) 164–173, <https://doi.org/10.1016/j.apenergy.2013.10.062>.
- [7] Y. Lu, J. Dong, J. Liu, Zonal modelling for thermal and energy performance of large space buildings: a review, *Renew. Sustain. Energy Rev.* 133 (2020), 110241.
- [8] E. Runkle, A.J. Both, *Greenhouse Energy Conservation Strategies*, 2011.
- [9] A. Vadiée, V. Martin, Energy management strategies for commercial greenhouses, *Appl. Energy* 114 (2014) 880–888.
- [10] M. Torrellas, A. Antón, M. Ruijs, N.G. Victoria, C. Stanghellini, J.I. Montero, Environmental and economic assessment of protected crops in four European scenarios, *J. Clean. Prod.* 28 (2012) 45–55.
- [11] M.J. Zarei, N. Kazemi, A. Marzban, Life cycle environmental impacts of cucumber and tomato production in open-field and greenhouse, *J. Saudi Soc. Agric. Sci.* 18 (3) (2019) 249–255.
- [12] J. Davis, Emissions of Greenhouse Gases from Production of Horticultural Products: Analysis of 17 Products Cultivated in Sweden, SIK Institutet för livsmedel och bioteknik, 2011.
- [13] M. Djévic, A. Dimitrijevic, Greenhouse energy consumption and energy efficiency, *Balk. Agric. Eng. Rev.* 5 (2004) 1–9.
- [14] M. Barozzi, J. Lienhard, A. Zanelli, C. Monticelli, The sustainability of adaptive envelopes: developments of kinetic architecture, *Procedia Eng.* 155 (2016) 275–284.
- [15] H.B. Awbi, *Ventilation of Buildings*, Routledge, 2002.
- [16] H. Andersson, M. Cehlin, B. Moshfegh, Experimental and numerical investigations of a new ventilation supply device based on confluent jets, *Build. Environ.* 137 (2018) 18–33.
- [17] T. Karimippanah, B. Moshfegh, On the performance of confluent jets ventilation system in office space, in: *Proceedings of Roomvent, 10th International Conference on Air Distribution in Rooms*, Finland, Helsinki, 2007.
- [18] K. Svensson, S. Ghahremanian, B. Moshfegh, M. Tummers, Numerical and experimental investigation of flow behavior in a confluent jet ventilation system



- for industrial premises, September 17-19, 2012, in: The 10th International Conference on Industrial Ventilation France, Paris, 2012.
- [19] K. Svensson, P. Rohdin, B. Moshfegh, A computational parametric study on the development of confluent round jet arrays, *Eur. J. Mech.* 53 (2015) 129–147.
- [20] S. Ghahremanian, K. Svensson, M.J. Tummers, B. Moshfegh, Near-field development of a row of round jets at low Reynolds numbers, *Exp. Fluid* 55 (2014) 1–18.
- [21] S. Ghahremanian, B. Moshfegh, A study on proximal region of low Reynolds confluent jets Part I: evaluation of turbulence models in prediction of inlet boundary conditions, January 18-22, 2014, New York, New York, USA, in: ASHRAE Winter Conference, vol. 120, 2014, pp. 256–270. Part 1, NY-14-021.
- [22] S. Ghahremanian, B. Moshfegh, A study on proximal region of low Reynolds confluent jets Part II: numerical verification of the flow field, New York, NY; United States; 18 January 2014 through 22 January 2014; Code 10631, in: 2014 ASHRAE Winter Conference, vol. 120, 2014, pp. 271–285. Part 1, NY-14-022.
- [23] S. Ghahremanian, B. Moshfegh, Evaluation of RANS models in predicting low Reynolds, free, turbulent round jet, *J. Fluid Eng.* 136 (1) (2014).
- [24] T. Arghand, T. Karimipannah, H.B. Awbi, M. Cehlin, U. Larsson, E. Linden, An experimental investigation of the flow and comfort parameters for under-floor, confluent jets and mixing ventilation systems in an open-plan office, *Build. Environ.* 92 (2015) 48–60.
- [25] T. Karimipannah, H.B. Awbi, C. Blomqvist, M. Sandberg, A.B. Fresh, Effectiveness of confluent jets ventilation system for classrooms, in: Proceedings of the 10th International Conference in Indoor Air Quality and Climate-Indoor Air, vol. 5, 2005, pp. 3271–3277.
- [26] Y. Cho, H.B. Awbi, T. Karimipannah, Theoretical and experimental investigation of wall confluent jets ventilation and comparison with wall displacement ventilation, *Build. Environ.* 43 (6) (2008) 1091–1100.
- [27] S. Janbakhsh, B. Moshfegh, Experimental investigation of a ventilation system based on wall confluent jets, *Build. Environ.* 80 (2014) 18–31.
- [28] L.L. Dong, C.W. Leung, C.S. Cheung, Heat transfer and wall pressure characteristics of a twin premixed butane/air flame jets, *Int. J. Heat Mass Tran.* 47 (3) (2004) 489–500.
- [29] V. Kolář, H. Takao, T. Todoroki, E. Savory, S. Okamoto, N. Toy, Vorticity transport within twin jets in crossflow, *Exp. Therm. Fluid Sci.* 27 (5) (2003) 563–571.
- [30] S. Janbakhsh, B. Moshfegh, Numerical study of a ventilation system based on wall confluent jets, *HVAC R Res.* 20 (8) (2014) 846–861.
- [31] H. Chen, S. Janbakhsh, U. Larsson, B. Moshfegh, Numerical investigation of ventilation performance of different air supply devices in an office environment, *Build. Environ.* 90 (2015) 37–50.
- [32] T. Karimipannah, A. Hb, B. Moshfegh, The air distribution index as an indicator for energy consumption and performance of ventilation systems, *J. Hum. Environ. Syst.* 11 (2) (2008) 77–84.
- [33] E. Tanaka, The interference of two-dimensional parallel jets: 1st report, experiments on dual jet, *Bull. JSME* 13 (56) (1970) 272–280.
- [34] D.R. Miller, E.W. Comings, Force-momentum fields in a dual-jet flow, *J. Fluid Mech.* 7 (2) (1960) 237–256.
- [35] S. Ghahremanian, B. Moshfegh, Numerical and experimental verification of initial, transitional and turbulent regions of free turbulent round jet, in: 20th AIAA Computational Fluid Dynamics Conference, 2011, p. 3697.
- [36] S. Ghahremanian, B. Moshfegh, Investigation in the near-field of a row of interacting jets, *J. Fluid Eng.* 137 (12) (2015).
- [37] H. Fatnassi, T. Boulard, H. Benamara, J.C. Roy, R. Suay, C. Poncet, Increasing the height and multiplying the number of spans of greenhouse: how far can we go?, *July, Acta Hortic.* 1170 (2017) 137–143, <https://doi.org/10.17660/ActaHortic.2017.1170.15>.
- [38] M. Duff, J. Towey, Two ways to measure temperature using thermocouples feature simplicity, accuracy, and flexibility, *Analog. Dialogue* 44 (10) (2010) 1–6.
- [39] R.H. Myers, D.C. Montgomery, C.M. Anderson-Cook, Response Surface Methodology: Process and Product Optimization Using Designed Experiments, John Wiley & Sons, 2016.
- [40] A.I. Khuri, S. Mukhopadhyay, Response surface methodology, *Wiley Interdiscip. Rev. Comput. Stat.* 2 (2) (2010) 128–149.
- [41] D.C. Montgomery, Design and Analysis of Experiments, John Wiley & Sons, 2017.
- [42] G.E.P. Box, D.W. Behnken, Some new three level designs for the study of quantitative variables, *Technometrics* 2 (4) (1960) 455–475.
- [43] J.S. Turner, J.S. Turner, Buoyancy Effects in Fluids, Cambridge university press, 1979.
- [44] J.J. Leonard, J.B. McQuitty, Archimedes number criteria for the control of cold, *Can. Agric. Eng.* 28 (2) (1986) 117–123.
- [45] D. Tan, B. Li, Y. Cheng, H. Liu, J. Chen, Airflow pattern and performance of wall confluent jets ventilation for heating in a typical office space, *Indoor Built Environ.* 29 (1) (2020) 67–83.